

# Vortex Method Simulation of Ground Vehicle Aerodynamics

**Peter S. Bernard**

University of Maryland and VorCat, Inc.

**Pat Collins and Mark Potts**

VorCat, Inc.

Copyright © 2004 SAE International

## ABSTRACT

Recent results are presented from the application of a grid-free vortex method to the prediction of turbulent aerodynamic flows produced by road vehicles. The approach has the character of a large eddy simulation and incorporates a fast technique for evaluating the mutual interactions of several million vortex elements needed in describing the dynamically significant structure of the turbulent field. The simulations provide information about the unsteady evolution of the flow including forces, vortical structure and separation regions. Predicted mean velocity statistics are shown to compare favorably with physical experiments.

## INTRODUCTION

Advances in supercomputing have brought Large Eddy Simulation (LES) techniques to the point where they represent a viable alternative to more traditional Reynolds-averaged Navier-Stokes (RANS) closures in modeling flows past ground vehicles [9,16]. Not only do LES schemes provide detailed transient information about forces, separation and wake structure that are absent in RANS methods [2,5,7,17], but they have the potential to provide substantially greater accuracy if for no other reason than that they make less demands on modeling per se. To a significant extent the advantages of LES can be further enhanced if a gridfree formulation based on the vortex method [12] is used in place of traditional gridbased schemes. In fact, vortex methods allow for a number of efficiencies and accuracies that are difficult to replicate within the confines of mesh based approaches. This paper describes some of the essential aspects of performing simulations of road vehicle flows using a gridfree scheme and then presents some results from computations of flows past generic automobile shapes that illustrate its capabilities.

The specific approach to be described is that developed by VorCat, Inc.<sup>1</sup> [3,4] in which convecting and stretching

vortex tubes are used as the principal computational element in conjunction with a thin mesh of triangular prism sheets, several layers thick, next to solid boundaries upon which the 3D vorticity equation is solved via a finite volume scheme. The wall calculation is highly resolved – approaching that typically seen in direct numerical simulations (DNS) – since this determines the location and strength of vorticity produced at the wall surface and then ultimately the vorticity field held on the gridfree elements.

Similar considerations in modeling the near wall flow apply in the case of traditional gridbased LES schemes. In fact, since all scales of motion next to boundaries are both energetic and subject to the effects of viscosity it is not evident that subgrid scale models are appropriate in this region. Rather, direct computation may be necessary if predictions are to be successful. For increasing Reynolds number the difficulty of employing adequate wall meshes is exacerbated. This often leads to the practice of imposing wall function boundary conditions that tend to be accurate under very limited circumstances. In the present case the boundary resolution problem is ameliorated to some extent because the thickness of the gridded region scales in wall units so it of necessity only increases with Reynolds number in two dimensions and not three. Secondly, the triangular prism elements are sheet-like and thus are efficient at providing coverage of the largely two-dimensional region of high vorticity next to boundaries.

There are several other features of the vortex method that provide advantages beyond that of gridbased methods. Thus, vortex tubes offer a substantially more efficient means of numerically representing physical vortices that are a dominant part of the dynamics of turbulent flow. Moreover, the convection and stretching of vortex elements can be accomplished without significant numerical diffusion so that sharp features of the flow, such as detached vortices and shear layers, remain sharp. Another useful aspect of vortices is that they provide an opportunity for imposing de facto “subgrid scale” models (that limit the resolution of vortices in the simulation) that are neither diffusive nor interfere with the natural process of backscatter by which

<sup>1</sup> The VorCat software is protected under U.S. Patent No. 6512999.

energy flows from small to large scales. Vortex methods are also naturally self-adaptive in the sense that they supply enhanced resolution to local areas of the flow as determined by the physics.

The next section describes some of the principal aspects of the gridfree methodology based on the vortex method. Following this is a discussion of some results taken from computations of the flow past the Morel [11] and Ahmed [1,10] bodies.

## GRIDFREE ALGORITHM

Vortex methods are gridfree numerical schemes for solving the 3D vorticity equation [3]

$$\frac{\partial \Omega}{\partial t} = -(\nabla \Omega)U + (\nabla U)\Omega + \frac{1}{R_e} \nabla^2 \Omega, \quad (1)$$

where  $U$  and  $\Omega$  are velocity and vorticity vectors, respectively, and  $R_e$  is the Reynolds number. The terms on the right hand side represent, in order, convection, vortex stretching and diffusion. Some of the particular considerations needed in solving (1) for a collection of tube elements and in a fixed mesh of triangular prisms adjacent to boundaries is now considered.

## TUBE ELEMENTS

Vortex tubes in the form of straight line segments form the gridfree computational element used in the VorCat code. Each tube is defined by its position as determined by its end points and its circulation  $\Gamma$ . The evolution of a tube is determined by the motion of its end points. In this way both the length and orientation of the tubes change in time. According to Kelvin's theorem, the circulation of a material vortex tube in an inviscid flow remains constant in time. This provides some justification - particularly in high Reynolds number flows away from boundaries - for assuming that  $\Gamma$  remains constant for each tube during its motion. Taken together these steps provide an approximation to the convection and stretching terms in (1) and it is thus seen that the dynamics of tubes is easily accommodated in the numerical scheme.

Associated with each vortex tube is the velocity field given by the approximate relation

$$U = -\frac{\Gamma}{4\pi} \frac{r \times s}{|r|^3} \psi(r/\sigma) \quad (2)$$

that is derived from the Biot-Savart law. Here  $r = x - x_c$  is the distance from a point  $x$  to the center of the tube,  $x_c$ , and  $s$  is an axial vector along the tube axis. Following the common procedure for vortex methods,  $\psi(r/\sigma)$  is a smoothing function that is used to desingularize the Biot-Savart kernel appearing in this relation.  $\sigma$  is a parameter that determines the size of the region over which the smoothing takes place. Beyond a distance proportional to  $\sigma$ ,  $\psi = 1$  and there is no smoothing.

As a flow evolves in time, there is a tendency for the tubes to increase in length as part of the natural process of vortex stretching. A maximum length of tubes is allowed and whenever tubes are longer than this they are subdivided. In this way, tubes that start out as single straight segments are likely to become chains of tubes forming filaments as time goes on. Note that such configurations may be viewed as discrete approximations to smooth physical tubes, so the shorter the tubes are allowed to be the more closely the discrete approximation follows the behavior of real tubes. There is a trade off between numerical efficiency and accuracy. Longer tubes are more computationally efficient but also less accurate. Generally, the maximum tube length is set as the average edge length of the triangles used in representing the boundary.

It may be seen in (2) that the velocity field associated with a vortex tube is proportional to the product  $\Gamma |s|$ . The value of  $\Gamma$  associated with a tube is determined at the time of its creation near the top of the wall mesh depending on local flow conditions and varies from tube to tube. It has been determined that discretization error is reduced if a bound is placed on the product  $\Gamma |s|$  so tubes are also subdivided according to this condition. This allows the strongest vortices to more naturally evolve in time (i.e., fold and stretch more responsively to local flow conditions).

Vortex tubes as computational elements have a significant capacity to mimic the true physical process by which energy cascades to small scales by vortex folding and stretching in spatially intermittent regions. For a vortex method to be practical it must restrain the growth in the number of tubes by modeling dissipation without trying to actually compute the complete folding and stretching process. The ways in which this is done in the code represent a de facto subgrid-scale model in VorCat. In essence, the idea is to eliminate those vortices whose future evolution can be expected to involve dissipation. Folding vortex tubes with the appearance of hairpins are associated with a primarily local velocity field [6] due to cancellation of the far field velocities produced by the oppositely rotating legs of the hairpin. If it can be assumed that the lengths of the tube segments are small enough - generally in the inertial subrange - then it is reasonable to identify the local energy associated with the hairpins as energy that is destined to be lost via viscosity after subsequent stretching and folding takes it to the dissipation range. Removing the hairpins eliminates the associated energy without the expense of a detailed calculation. This is similar to the effect that subgrid scale models have in mesh based schemes in removing energy traveling to unresolved scales.

Another aspect of the present subgrid scale modeling is contained in the idea that the vortices, even if they do not form tight hairpins, tend to stretch rapidly in many instances. As they stretch so too does the material volume that they occupy. For volume to be conserved the thickness of the tubes must shrink as they get longer. It should be noted that the tube area in this instance is

understood implicitly and is not an actual parameter in the computations. After an individual tube has stretched and been subdivided many times, it is to be expected that its associated thickness is reduced to the scale of the dissipation range, and if so, the corresponding tube can be eliminated on the belief that its coherent vorticity would have been smoothed away by viscosity. Between hairpin removal and the elimination of highly subdivided tubes, the population of vortices is prevented from increasing so rapidly as to render the method impractical.

## VORTEX PRISMS

Solid surfaces are represented in VorCat through triangularizations. The triangular mesh used in the computation of the wall flow is grown out from the boundary triangles by erecting perpendiculars at the node points. The number of layers is usually taken to be 11. The first layer is of half-thickness, say  $\Delta y/2$ , where  $y$  is the direction normal to the boundary. Each of the remaining layers are of thickness  $\Delta y$ . The vorticity is assumed to be constant over each triangular prism.

The vorticity components at the wall surface represent boundary conditions for the computation of vorticity in the sheets. These are evaluated via finite difference approximations using the no-slip condition on the solid surface. It is thus important that  $\Delta y$  be small enough that these approximations are accurate.

The thickness of the region near the wall surface that needs to be covered by triangular prisms is an important consideration in the present methodology. It must be large enough to fully encompass the high vorticity and its gradients that are produced next to solid walls via viscosity. This region generally constitutes the viscous sublayer and an immediately adjacent part of the turbulent boundary layer. Here there is a large viscous flux of vorticity out of the solid surface leading to the appearance of vorticity in the flow. The vorticity field in the mesh is determined as a solution to (1) via a finite volume scheme. The result of the computation is to establish the amount of vorticity that convects and diffuses to the top sheet layer, to subsequently be turned into new vortex tubes.

For a given Reynolds number the thickness of the sheet region is targeted to be within  $y^+ = 25 \rightarrow 50$ , where  $y^+ = U_\tau y/\nu$  denotes wall coordinates and  $U_\tau$  is the friction velocity. To utilize approximately 11 sheet levels, it is generally required that  $\Delta y^+$  be taken to be approximately 3. This places the sheet resolution in the normal direction at the high end of what may be appropriate for DNS and allows for a reasonable determination of the wall vorticity via a finite difference approximation.

The sizes, dimensions, and overall compartment of the surface triangles can have a significant effect on the accuracy and performance of the finite volume scheme. For example, long narrow triangles need to be avoided. An especially important aspect of the mesh is the

average aspect ratio defined as the average edge length of the triangles divided by  $\Delta y$ . The larger this ratio is the coarser the spanwise resolution is and the more likely that there will be significant discretization error. On the other hand, the smaller the aspect ratio the more triangles are needed to cover a surface and the more expensive the computation becomes. There is also a lower limit for the aspect ratio since the triangular prisms must be "sheet-like" in order to use velocity formulas that have been developed with this condition in mind. It is found empirically that an aspect ratio of 10 is perhaps ideal. If  $\Delta y^+ \approx 3$  and the triangular prisms have an average aspect ratio of 10, then the typical spanwise extent of the triangles is about 30 wall units, which is adequate for resolving streamwise vortical wall structures directly in terms of the vorticity field.

## FINITE VOLUME ALGORITHM

The vorticity field is determined in the mesh region via a finite volume solution to the 3D vorticity equation. For each triangular prism the vorticity is that at its center, while the velocities are computed at the centers of the top and bottom triangles. The velocities at the six nodal corners of the prism are determined via area-weighted averaging of the velocities at the centers of the top and bottom triangles. The finite volume scheme uses a simple explicit time discretization. The convection term is approximated by applying the divergence theorem to its equivalent conservative form yielding an expression for the net flux of vorticity from a prism as a sum of contributions from each of its five sides. For this calculation the vorticity on the triangular faces is taken from the upwind prism. On the quadrilateral sides the vorticity is taken from a linear least square fit of the vorticities in prisms that are contiguous to the prism on the upwind side of the surface on the same and the immediately neighboring levels above and below, plus the one prism on the downwind side.

The evaluation of the stretching term is done at the center of the prisms so the vorticity appearing in the expression is directly available. The velocity gradient is computed using the scalar divergence theorem following a similar approach as done in computing the convection term.

The evaluation of the diffusion term in (1) distinguishes between diffusion normal and parallel to the surface. The Laplacian is expressed in a local rectangular Cartesian coordinate system and the term with normal derivatives is evaluated using a standard second order finite difference formula using the vorticity values at the centers of the prisms. The two tangential terms are computed by differentiation of a polynomial determined by a second order least-square fit of the vorticities of prisms located within a given radius of the prism center and in the layers immediately above and below the prism.

Several aspects of the time integration are noteworthy. First of all, the time step  $\Delta t$  is limited by CFL conditions in

the normal and tangential directions as well as a diffusive stability requirement. In practice  $\Delta t$  satisfying these conditions is smaller than it would have to be in order to compute accurate motion of the vortex tubes. Consequently, a number of iterations of the finite volume scheme, referred to as subcycles, are performed before updating the positions of the vortex tubes. The contribution of the vortex tubes to the velocities in the mesh is held fixed during the sub-cycling.

To solve the finite volume equations a boundary condition is needed for the vorticity at the top sheet level. An effective approach in this regard is to solve the finite volume equations only up to the second to last sheet level assuming the viscous flux in the wall normal direction to be constant over this sheet. A calculation of the total vorticity flux due to convection and diffusion into the top sheet level supplies the vorticity that is put into new tubes. In this, when the convective flux is away from the surface the vorticity at the top sheet is not needed (in view of the upwind model), while if the flux is toward the surface it is taken to be zero since all incoming vorticity is expected to be in the form of vortex tubes.

The finite volume algorithm described here is found to offer stable solutions to the 3D vorticity equation over a wide range of flows that have been treated thus far. Moreover, tests have shown each separate part of the numerical discretization to be consistent and convergent under mesh refinement.

## NEW VORTICES

Going hand in hand with the computation of the evolving vorticity field in the wall mesh is the necessity of collecting information on the amount of vorticity that fluxes outward into the top level of prisms. The flux derives from both viscous and convective components. The vorticity that accumulates during the time steps in the sub-cycling is turned into a vortex tube if its magnitude surpasses a threshold. The orientation of the new vortex is clear from the relative magnitudes of the vorticity components. Its center is at the center of the prism whose vorticity it will take. The length of the new tube is set by the condition that its ends just intersect the sides of the prism. Its strength is determined via the relation

$$\Gamma |s| = |\Omega| V \quad (3)$$

in which  $V$  is the volume of the prism. This condition forces the far field velocity from the new tube to match that of the prism.

## VELOCITY EVALUATION

According to the Helmholtz decomposition theorem the velocity in incompressible flow can be written as the sum of a divergence free part and a potential flow that enforces the non-penetration boundary condition. For a given vorticity field  $\Omega$  the solenoidal part takes the form of the Biot-Savart law

$$\mathbf{U}(x, t) = -\int \frac{(x - y) \times \Omega(y, t)}{|x - y|^3} dV \quad (4)$$

This forms the basis for (2) in the case of tubes, and for the prisms it is integrated in closed form over the two lateral directions assuming constant vorticity. Since the prisms have high aspect ratio a simple midpoint approximation is used for the integration in the normal direction. In view of the expense of evaluating the complex formulas that result from integration of (4), they are used only in the near field. Elsewhere, the velocity due to the prisms is computed assuming an equivalent vortex tube with strength given by (3). The potential flow is determined via a boundary element method that makes use of the surface triangularization. Thus the computation of the complete velocity field is done without imposition of a grid covering the flow domain.

The locations where the velocity field is to be evaluated are known as "field points." These may be considered to be of three types: 1. the end points of vortex tubes not located within the mesh region; 2. the end point of tubes that are in the mesh region; and, 3. the centers of the triangles in the wall mesh. The contribution of the vortex tubes to all categories of field points is the same: they are evaluated using a parallel implementation of the Fast Multipole Method (FMM) [8,14]. The contribution of the sheets to the first and third category of mesh points is via the local or far field velocity sheet formulas as may be relevant. For the second category of points, however, the velocity contributed by the sheets is computed via a combination of interpolation and least square fitting. In particular, the velocities from the third category are used to estimate the velocities at the node points using area weighted averaging. To then get the velocity for the end point of a tube that lies in a particular prism, a least-square fit is done using the six nodes of the prism. A motivation for this special approach is to enhance efficiency since the evaluation of the local sheet formulas for large numbers of vortices can be expensive. It is also the case that this approach reduces some discretization error, particularly in the normal velocity component that arises from the assumption of piecewise constant vorticity over coarsely sized triangles.

There are three separate calls to the FMM solver in the velocity computation. The first is for the purpose of evaluating the contributions of the tubes at all field points. In this the flow domain is covered by an oct-tree whose boxes, in principle, should be subdivided adaptively until there is an optimal number of tubes in each box (approximately 100). Regions containing greater numbers of tubes undergo more subdivisions than others. A tube is placed into a box according to the location of its center point. A similar oct-tree is developed for the field points. The two trees are similar but might not be identical. The best performance of the FMM can be expected to occur when the oct-trees have been grown to their optimal levels.

The FMM works by combining the influence of tubes in a particular box into a single multi-pole expansion, and then gathering such expansions together for parent boxes that hold smaller "child" boxes. Similarly, expansions used in computing field points are brought from parent to child boxes down through the tree. Adjacent boxes at the smallest size affect each other only through the exact formulas, that is, such interactions cannot be included in the multipole expansions. For this reason, having more than the optimal number of tubes in a box can hamper efficiency of the FMM solver.

In its application to computing the velocity due to tubes, it is generally not the case that the oct-trees can be grown to their optimal levels. Preventing this is the need to smooth the Biot-Savart kernel at small distances: the FMM depends on the unsmoothed kernel for its derivation. To maintain the effectiveness of the FMM in cases where many particles accumulate in the smallest boxes, a "middleman" scheme is used in which the FMM is used to evaluate the velocities at certain nodal points within the boxes and then 3D linear interpolation is used to get the velocities at the field points in these boxes. Typically, the nodal points are the corners of boxes constructed by two further subdivisions of the smallest boxes in the FMM oct-tree.

The second call to the FMM is for contributions of sheets. In this case the positions of tubes lying within the mesh region are excluded from the field points. For this calculation the standard Biot-Savart kernel is used for non-near neighbor boxes while the integral formulas for triangles are used to compute the local contributions. Finally, the last call to the FMM is for the purpose of computing the contributions of the wall sources to the velocity field.

The use of the FMM reduces the nominal  $O(N^2)$  cost of evaluating the velocities at the locations of  $N$  vortices to a much more affordable  $O(N \log(N))$  or even  $O(N)$  calculation. With parallelization, problems containing several million vortices can be treated in a reasonable time frame. For example, with 4 million vortices, the VorCat code maintains excellent parallel scalability through at least 16 processors, with scalability increasing as the number of vortices increases. In a typical result, a calculation with 4 million vortices on 64 processors takes under 1 minute of CPU time. This is sufficient to enable useful calculations for many complex flows in a reasonable time.

## RESULTS

The previously described algorithm has been applied to a number of ground vehicle flows with a view toward establishing its accuracy and physical correctness. This work is ongoing in the sense that most of the computations have yet to be performed at Reynolds numbers of  $O(10^6)$  that are typical of experimental studies of the Ahmed and Morel body flows. In particular, triangularizations appropriate to high Reynolds number flow entail  $O(10^5)$  surface triangles and several million

prisms to achieve a fine coverage of turbulent structures next to boundaries. Such computations can be expected to produce  $O(10^8)$  tubes and thus require a significant investment in computational resources (e.g., a larger number of parallel processors than are typically available for this developmental work).

In the interest of more rapidly exploring the performance of the scheme over a wide range of cases the present results have been obtained from simulations with approximately 500,000 prisms and several million vortex tubes. These more modest computations can be completed within a day or two using 16 or 32 processor parallel computers. The results given here are for Reynolds numbers no greater than 500,000 since this is the upper limit for which a surface mesh containing approximately 30,000 triangles can provide resolution that is at least adequate for representing the physics of the viscous sublayer.

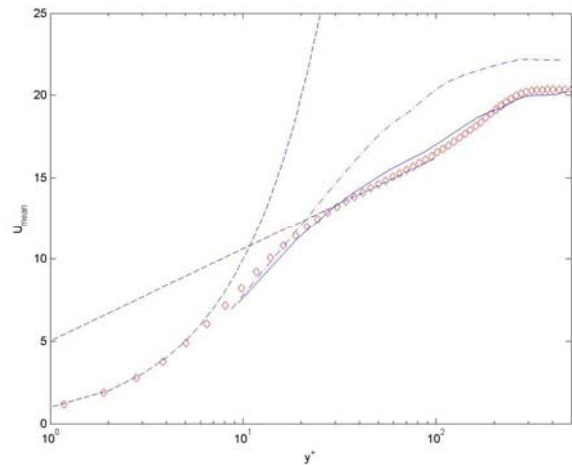


Figure 1.  $U^+$  at  $Re=360,000$ .  $\diamond$ , DNS from [13]; —, gridfree scheme with fine mesh; - · -, gridfree scheme with coarse mesh.

## BOUNDARY LAYER

The particular issue of surface resolution has been studied via analysis of the velocity statistics of the turbulent boundary layers that form on the top and bottom surfaces of the Morel and Ahmed bodies. For example, Fig. 1 is a comparison of the mean velocity scaled in wall coordinates as computed from a Morel body at  $Re = 360,000$  (based on streamwise body length) compared to a DNS calculation [13] and the classic log law relation  $U = 1/0.41 \log(y^+) + 5$ . In this discussion  $(x,y,z)$  respectively denote the streamwise, normal and transverse coordinates. The DNS solution has Reynolds number based on momentum thickness  $Re_\theta = 500$ , and the computed solution has  $Re_\theta = 622$ . Both a coarse mesh and a fine mesh solution are shown, with the latter used just on the top surface of the body to limit the overall number of triangles. It is seen that in this instance the better resolution makes a significant difference in so far as the accuracy of the prediction is concerned. The different mesh characteristics are

reflected in their spanwise resolution. For the fine mesh on average  $\Delta z^+ = 107.2$  with aspect ratio 16.3, while for the coarse mesh  $\Delta z^+ = 240.4$  with aspect ratio 36.9. Even though the fine mesh is less than ideal, it is still seen to produce a mean flow that is consistent with that of a turbulent boundary layer and, in fact, has a clear log law. In contrast, the coarser mesh is prone to significant error. For both computations,  $\Delta y^+ \approx 6.5$ . The results for the Ahmed body flow presented below are obtained using meshes (depending on Reynolds number) that vary between the coarse and fine resolutions seen here.

The normal Reynolds stresses corresponding to the mean velocity in Fig. 1 are somewhat over predicted as shown in Fig. 2. With better resolution these statistics improve. For example Figs. 3 and 4 show results for the mean velocity, Reynolds shear stress and turbulent kinetic energy for a better resolved simulation at  $Re = 64,800$ . The first two statistics are excellent. The displacement in peak kinetic energy away from the wall may reflect the need for yet an additional enhancement to the wall resolution or may be due to differences between the Morel body and boundary layer flows.

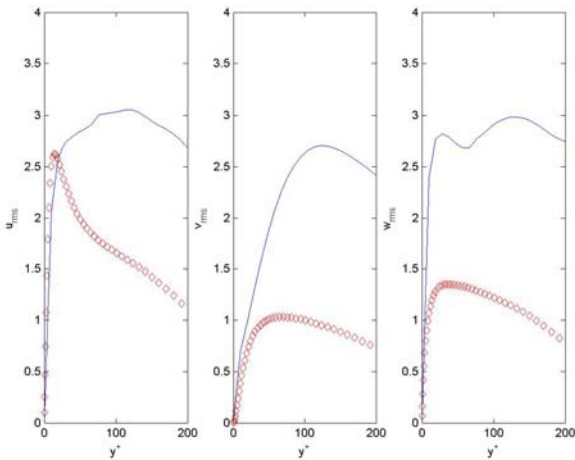


Figure 2. Normal Reynolds stresses for  $Re=360,000$  boundary layer.  $\diamond$ , DNS from [13]; —, gridfree scheme.

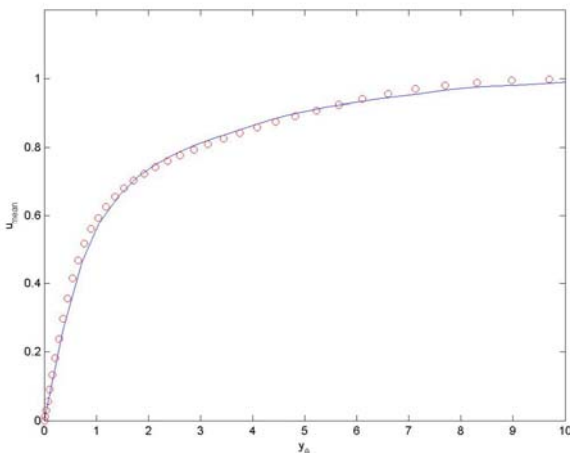


Figure 3. Mean U at  $Re=64,800$ .  $\diamond$ , DNS from [13]; —, gridfree scheme.

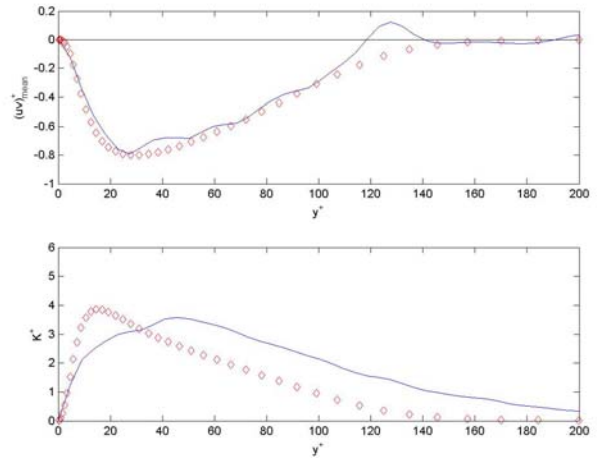


Figure 4. Reynolds shear stress and turbulent kinetic energy for boundary layer at  $Re=64,800$ .  $\diamond$ , DNS from [13]; —, gridfree scheme.

### AHMED BODY FLOW STATISTICS

Several calculations have been made of the Ahmed body flow including an inviscid rather than viscous ground plane. Though this prevents the simulation from including the effect of vorticity generated on the floor of the wind tunnel, it has the advantage of reducing the scale of the computations while still allowing for meaningful comparisons with experiments. A viscous ground plane will be included in future computations of the Ahmed body flow. Some idea of the quantitative accuracy of the approach is obtained by comparing computed and measured mean velocities and Reynolds stresses for the case with  $25^\circ$  base slant angle. The computations are for  $Re = 500,000$ , a value that is at the upper limit of what can be tolerated with available computer resources, but still less than the value  $Re = 2,784,000$  used in experiments. In the computations the Ahmed body is represented using a surface mesh containing 32,432 triangles with an additional 3920 triangles on the ground plane. With 10 layers of prisms above the surface prisms there are thus 324,320 total. *A posteriori* it is determined that the average prism in the simulation has thickness 12.8 in wall coordinates and average spanwise extent of 280. While this surface mesh is clearly less than optimal as suggested by the boundary layer results, nonetheless the predicted statistics show much agreement with the physical experiments. This is now illustrated in a number of comparisons for streamwise, normal and transverse mean velocities,  $U$ ,  $V$  and  $W$ , respectively, turbulent kinetic energy,  $K$ , and Reynolds shear stress,  $\overline{uv}$ , at various locations situated along the centerline of the body and above the rear window. The numerical calculation is run from an impulsive start until approximately  $t = 1.5$  with averaging performed over essentially the last 0.5 time units. The front surface of the body is at  $x = 0$ , the rear is at  $x = 1$ , the ground plane is at  $y = 0$ , and the bottom and top surfaces of the Ahmed body are at  $y=0.04675$  and  $0.3253$ , respectively. Moreover, the body extends in the spanwise direction

from  $z = -0.1874$  to  $0.1874$  and the rear slanted window begins at approximately  $x = 0.837$  and ends at  $x = 1$ .

Figures 5 - 8 pertain to the mean streamwise velocity,  $U$ , while Figs. 9 – 12 are for  $V$ . Figures 5 and 9 are for locations on the centerline in front of the body and on the top surface. Ahead of the body the close agreement between experiment and computation reflects the more or less potential nature of the flow in this region. Near  $y = 0$  the effect of using an inviscid boundary is visible. The plots for  $x > 0$  show that the acceleration of the fluid over the top surface is captured as well as the boundary layer profiles over the rear window. In these results it can be expected that the modeling of the turbulent physics plays a role. It may also be noticed that the qualitative agreement with experiment is quite good, in addition to the quantitative accuracy.

The predicted wake characteristics on the centerline are shown in Figs. 6 and 10. Just downstream of the body, at  $x = 1.0364$  the wake profile is fairly well captured including the recirculating zone. The comparisons further downstream suggest that the extent of the wake deficit is smaller than experiment. It may be expected that a number of factors contribute to this disparity, with the most obvious being the smaller Reynolds number of the simulation in comparison to experiment. This is supported by a calculation at  $Re = 100,000$  that was observed to have a smaller wake deficit than the calculation at higher Reynolds number. The flow in the wake is highly non-steady and it is clear that the averaging interval that is used here to obtain statistics is not sufficiently long to produce entirely smooth results. In fact, this limitation is felt most strongly in the last few measurement stations and may also have some responsibility for the smaller than measured wake deficit. For example, it may be inferred from the last plot in Fig. 10 that the vortices produced by the body have barely reached this location by the end of the simulation.

Figures 7 and 8 for  $U$  and Figs. 11 and 12 for  $V$  illustrate the quality of the computed solution at different spanwise locations at two different  $x$  positions centered over the rear window. Many details of the boundary layer in this region appear to be well captured. It is interesting to note that the profiles at  $z = 0.21073$  are just off to the side of the body. These are embedded in the turbulent, separated boundary layer that is generated on the side of the vehicle. These curves are clearly quite noisy and require a longer averaging interval to produce smooth statistics. Figure 13 shows  $W$  at three  $z$  locations on either side of the body. This plot demonstrates that the average flow over the window is toward the centerline, as is expected in the case of the  $25^\circ$  base slant angle.

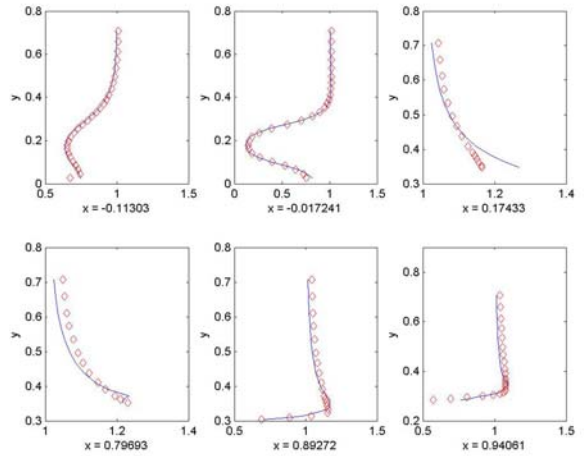


Figure 5 Computed streamwise velocity on centerline, —; vs. experiment [10],  $\diamond$ .

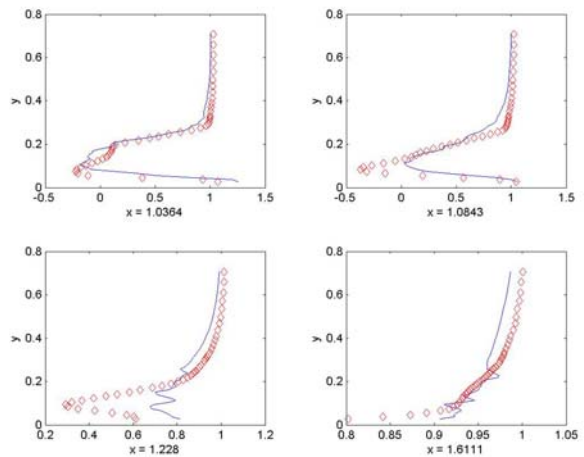


Figure 6. Computed streamwise velocity on wake centerline, —; vs. experiment [10],  $\diamond$ .

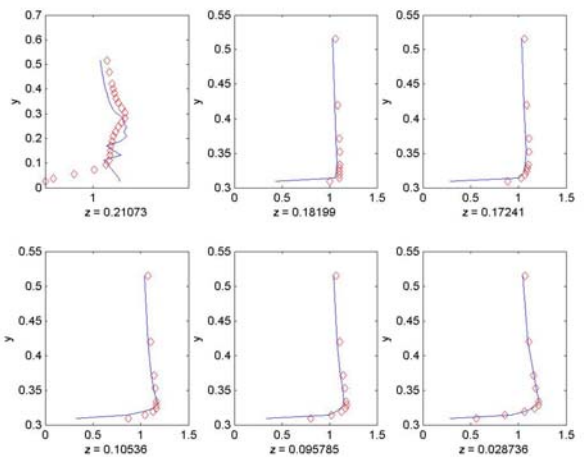


Figure 7. Computed streamwise velocity at spanwise locations at  $x = 0.8678$ , —; vs. experiment [10],  $\diamond$ .

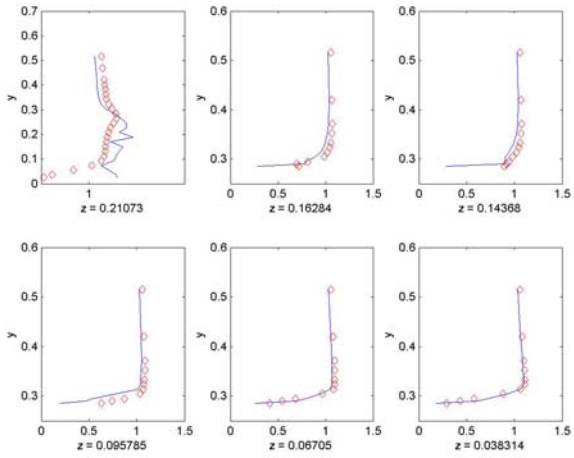


Figure 8. Computed streamwise velocity at spanwise locations at  $x = 0.9157$ , —; vs. experiment [10],  $\diamond$ .

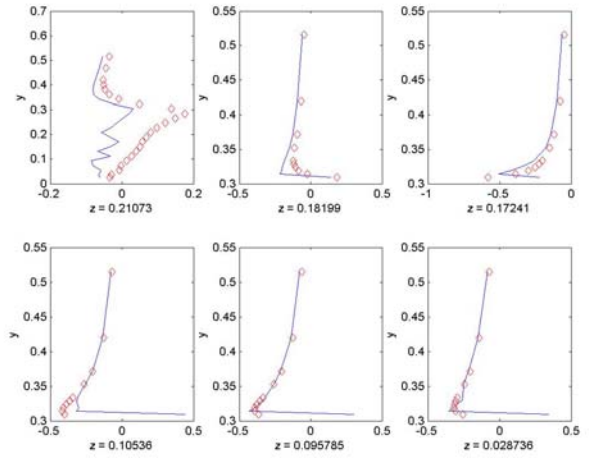


Figure 11. Computed normal (V) velocity at spanwise locations at  $x = 0.8678$ , —; vs. experiment [10],  $\diamond$ .

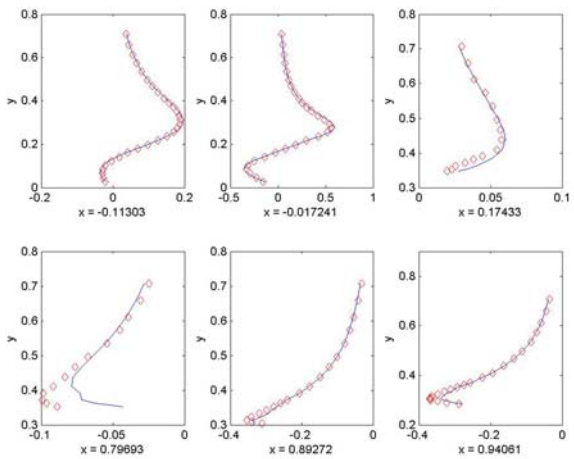


Figure 9. Computed normal (V) velocity on centerline, —; vs. experiment [10],  $\diamond$ .

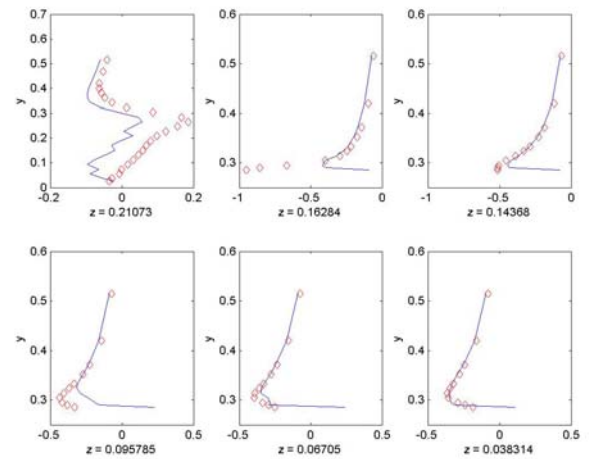


Figure 12. Computed normal (V) velocity at spanwise locations at  $x = 0.9157$ , —; vs. experiment [10],  $\diamond$ .

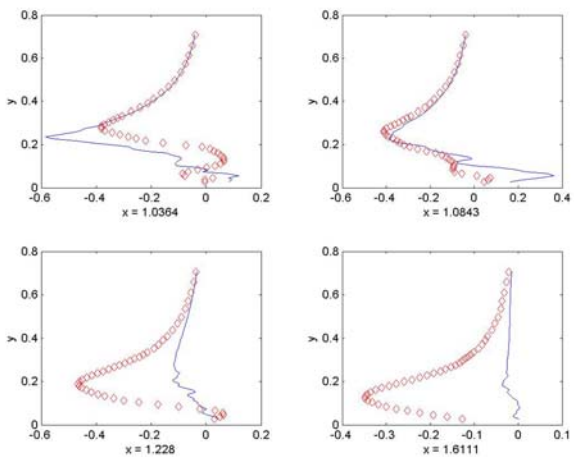


Figure 10. Computed normal (V) velocity on wake centerline, —; vs. experiment [10],  $\diamond$ .

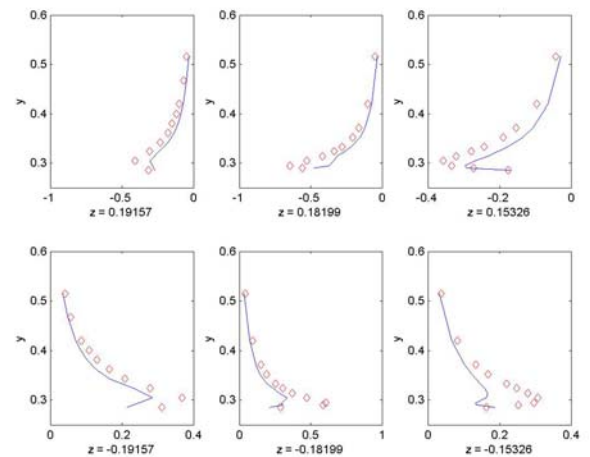


Figure 13. Computed transverse (W) velocity at spanwise locations at  $x = 0.8678$ , —; vs. experiment [10],  $\diamond$ .



Figure 14 compares the predicted  $K$  vs. experiment at points along the centerline. The first two locations are over the window and the remaining four are in the wake. The accuracy of the individual curves varies somewhat from location to location with some trends quite accurately captured. There is a clear need for longer averaging to produce smoother statistics and this might have some effect on the uniformity of the predictions. In fact, it is not hard to imagine that higher order statistics such as  $K$  are particularly vulnerable to the influence of individual large scale flow events if the averaging is over too short a time interval. In any case, it is interesting to note that the double-peaked  $K$  distribution in the near wake is well reproduced, particularly at  $x = 1.0364$ . Figures 15 and 16 show  $K$  for locations over the rear window. Here, more averaging is clearly required if the accuracy of the predictions is to be carefully evaluated. A clear trend toward over prediction is visible in these results. This is perhaps related to the use of an overly coarse surface mesh, very much like the situation previously encountered in regards to Fig. 2.

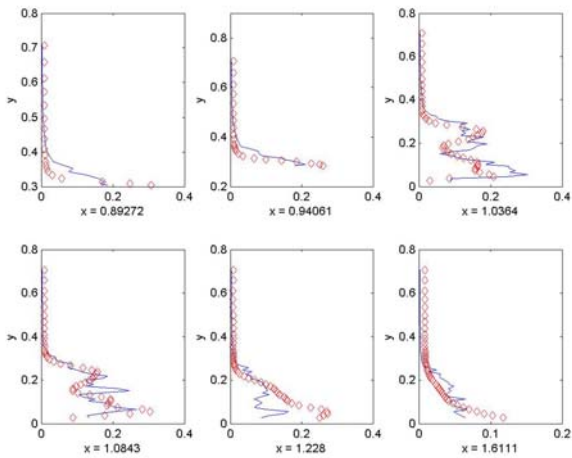


Figure 14. Computed turbulent kinetic energy on centerline, —; vs. experiment [10],  $\diamond$ .

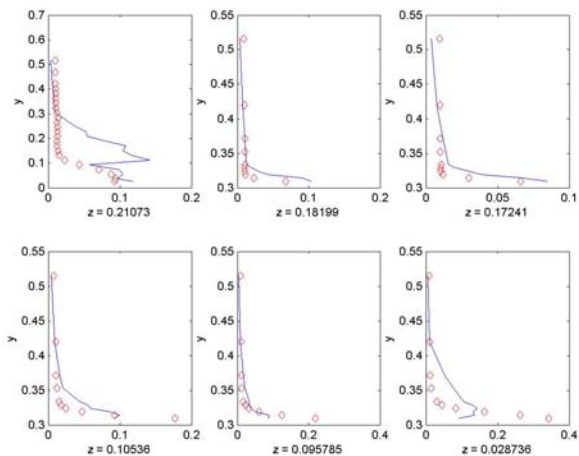


Figure 15. Computed  $K$  at spanwise locations at  $x = 0.8678$ , —; vs. experiment [10],  $\diamond$ .

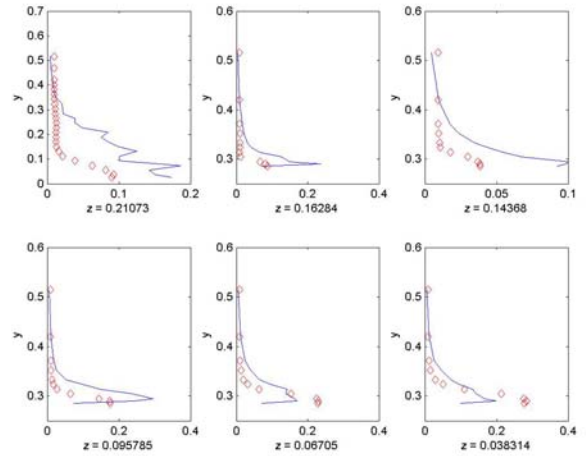


Figure 16. Computed turbulent kinetic energy at spanwise locations at  $x = 0.9157$ , —; vs. experiment [10],  $\diamond$ .

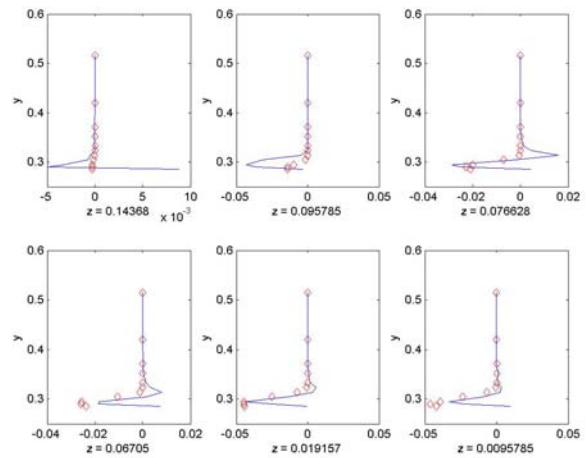


Figure 17. Computed Reynolds shear stress at spanwise locations at  $x = 0.9157$ , —; vs. experiment [10],  $\diamond$ .

The Reynolds shear stress predictions in the middle of the rear window are shown in Fig. 17. The numerical model clearly is able to reproduce the preferential correlation that underlies  $\overline{uv}$  as was previously seen in Fig. 4. This generally requires that the vortical structures of turbulence that cause the Reynolds shear stresses are correctly accounted for in the simulation. More insight into this aspect of the solution can be achieved by visualizing the gridfree vortical elements that make up the flow, as will now be considered.

## VISUALIZATIONS

Visualization results are shown primarily for a relatively well resolved computation in which the base slant angle is  $30^\circ$  and the Reynolds number  $Re = 40,000$ . In this calculation there are 28,538 triangles on the vehicle surface. Three-dimensional renderings of the vortices give an indication of separation regions and the locations and degree of turbulence production. Such views often

show where many small vortices have combined to form larger scale structures that might be of interest. It is also possible to obtain information about the origination on the body of vorticity appearing in the wake.

Shown here in Figs. 18 - 20 are images at time  $t = 1.91$  of the approximately 2.5 million vortex tubes that have been generated in the course of a calculation of the Ahmed body flow impulsively moved from rest at  $t=0$ . The figures respectively show views from the side, the front and the top. Both Figs. 18 and 20 show boundary layers forming from the leading edge of the body, their downstream transition to turbulence, and the formation of turbulent structures. The latter are most visible in the large mainly streamwise agglomerations of vortices as well as the corrugated outer edges of the vortex layers. Such structures are consistent with the known characteristics of turbulent boundary layers and help explain the good agreement in predicting velocity statistics shown previously. Another perspective on the flow is given in Fig. 21 showing contours of normal velocity just above the top surface of the body. There is clear evidence here for the existence of the streaky structure that is the footprint of coherent streamwise vortices in boundary layer flow [5].

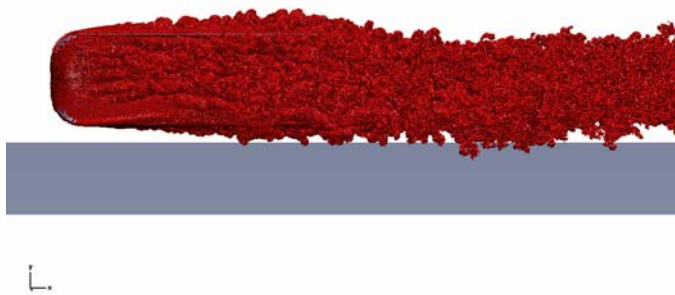


Figure 18. Side view of vortices in Ahmed body flow.



Figure 19. Front view of vortices in Ahmed body flow.

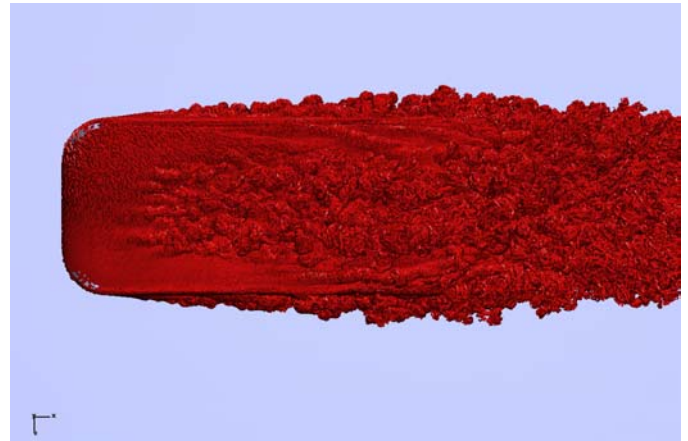


Figure 20. Top view of vortices in Ahmed body flow.

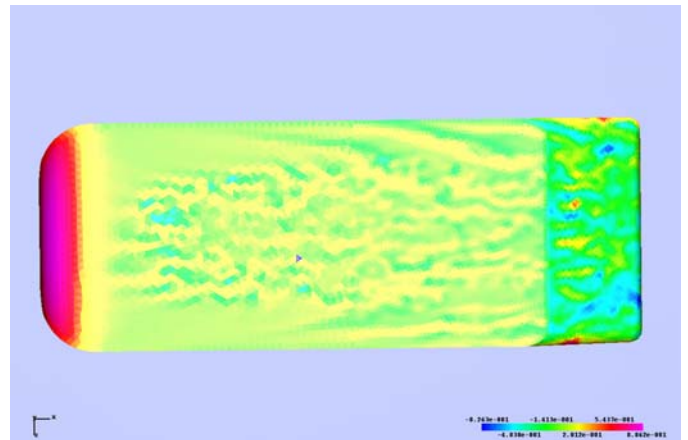


Figure 21. Wall normal velocity above top surface of the Ahmed body.

The flow over the rear window is an important feature of the Ahmed body flow. Instantaneous quiver plots of velocity vectors in planes parallel to the symmetry plane are shown in Figs. 22 and 23 for base slant angles of  $12.5^\circ$  and  $30^\circ$ , respectively. In the former case there is no separation over the window, though a large recirculating vortex forms against the rear. These results are consistent with the known behavior of the flow at this angle. For the larger angle there is clearly a considerable degree of separation over both the rear window and back. Animations of the velocity field show the separated flow regions to vary rapidly in time and spatial position. Once again the behavior is consistent with the high drag configuration of the Ahmed body that occurs at base slant angles in the vicinity of  $30^\circ$ .

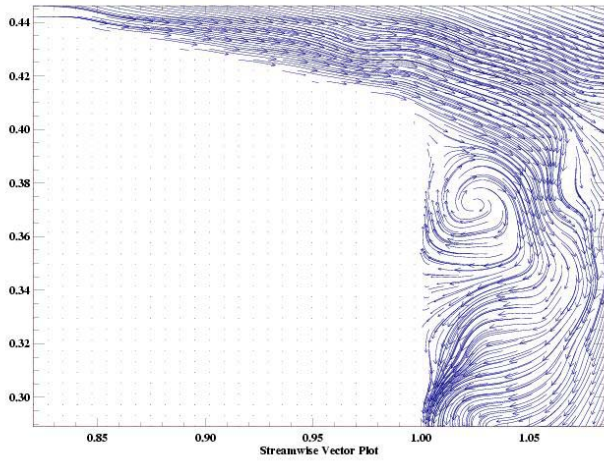


Figure 22. Instantaneous velocity vectors over the rear of the Ahmed body at 12.5° base slant angle.

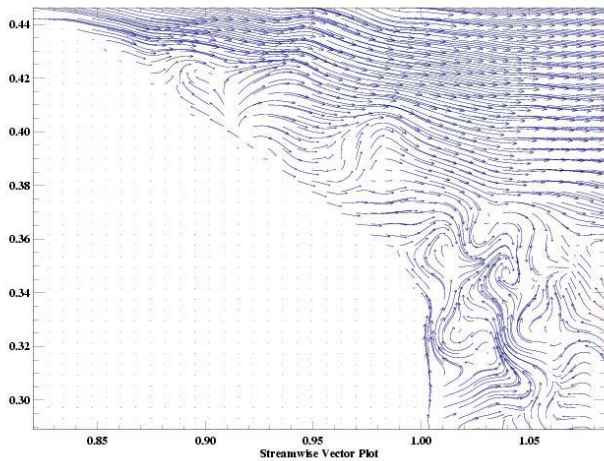


Figure 23. Instantaneous velocity vectors over the rear of the Ahmed body at 30° base slant angle.

Some insights into the vortical nature of the flow over the window may be obtained from Figs. 24 and 25. The former shows contours of streamwise vorticity close to the body surface in which there is a clear pattern of alternating sign in the vorticity just as the flow moves over the window. This hints at the presence of some spanwise structure to the separated flow at this location, not unlike similar phenomena in mixing layers [4]. The visualization of vortices in Fig. 25 gives some evidence of the vortical flow over the C-pillars. This turbulent state has evolved from the situation shown in Fig. 26 that is not long after the start up of the calculation and before the flow has transitioned to turbulence. Here the vortices are clearly seen to curl over the C-pillars. It is also interesting to note the rollup of the vorticity shedding off the bottom rear edge of the body.

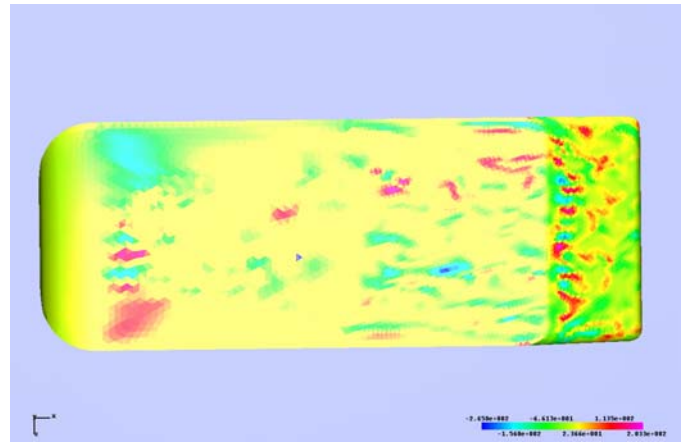


Figure 24. Streamwise vorticity contours on the top surface of the Ahmed body flow.

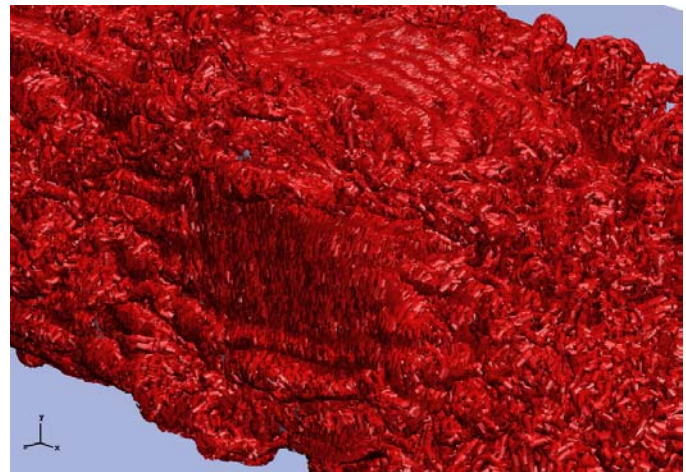


Figure 25. Detail of vortices near the rear window at an early time showing wrapping of vortices over the C-pillars.

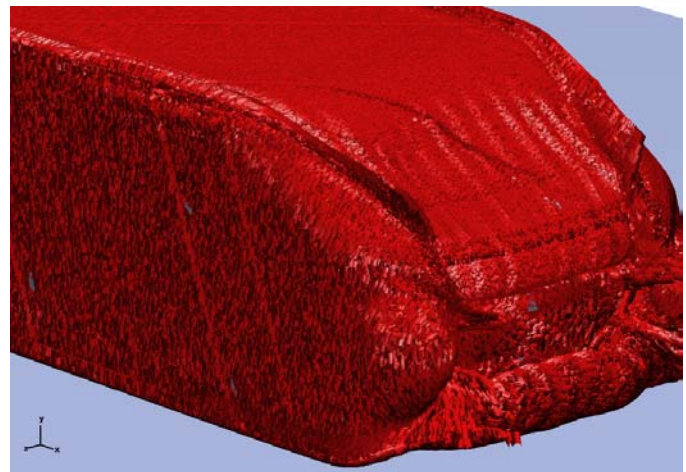


Figure 26. Vortices shed off rear shortly after startup of the simulation.

## FORCES

The pressure in a vortex method is determined at any fixed time step as a post-processing step using the instantaneous vorticity distribution that is contained in the tubes and prisms. A particularly convenient way to get pressure on the solid viscous surfaces appearing in a computation is by an application of Green's third identity [15]. Due to the appearance of a singularity in the Green's function, however, some care must be given to how the numerical quadrature is carried out. For example, the computed pressure can be a sensitive function of the evolving vorticity field, and if so, relatively long time averages are needed to get mean pressures. Integrated quantities depending on pressure such as the drag coefficient are less affected by transient fluctuations.

In the present case a higher order pressure solver that is useful for obtaining local pressure fields is in the final state of development and results from this will be reported in the future. A less accurate, preliminary pressure solver has been developed in order to verify the concept. This is useful for obtaining integrated quantities such as drag but requires long time averaging to get converged pressure statistics. Fig. 27 shows the computed drag force for the 30° Ahmed body as a function of time. To the extent that a comparison can be made between flows at quite different Reynolds numbers, it may be noted that the value in the figure at the last time is in the vicinity of 0.42 and this may be contrasted with the experimental value of 0.36.

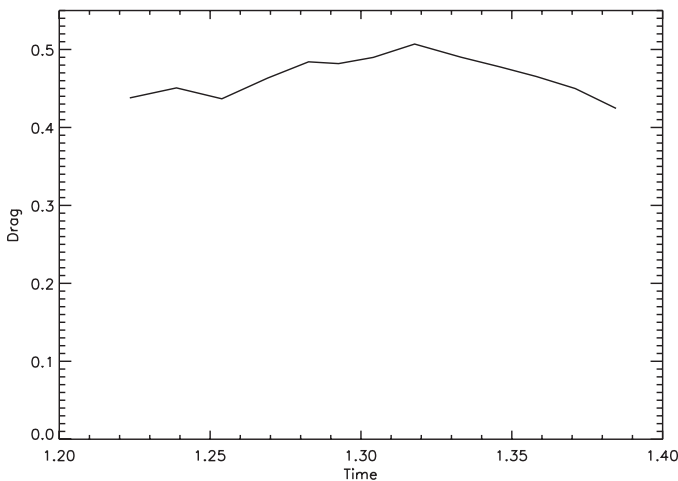


Figure 27. Time dependence of computed drag coefficient for 30° Ahmed body simulation at  $Re = 40,000$ .

## CONCLUSION

The computational results presented here demonstrate some of the capabilities of a gridfree approach to large eddy simulation in modeling ground vehicle flows. While many of the difficulties of grid generation that typically affect LES schemes are avoided in this work, the study does show the importance of having a reasonably fine

near-wall mesh to resolve the important vorticity producing motions upon which the gridfree elements depend. The wall resolution issue reflects the fact that with the absence of a turbulence model per se, the Reynolds number is a real parameter in this method and its effect on the physics has to be taken into account where necessary.

The present computations demonstrate that quantitatively accurate predictions of velocity statistics can be obtained as long as appropriate wall resolution is maintained. The simulations are seen to provide a wealth of visual information about the nature of the turbulent and rotational motions produced by ground vehicles. Future computations will be focused on scaling up the simulations to exactly match the conditions of experiments. This is primarily a question of securing computational resources commensurate with the large storage requirements for simulations containing ten million or more vortices and several million wall prisms.

## ACKNOWLEDGMENTS

This research has been supported through an ATP/NIST award to VorCat, Inc. Computer time is provided in part by NCSA.

## REFERENCES

1. Ahmed, S. R., et al. (1984) Some salient features of the time-averaged ground vehicle wake, SAE Paper No. 840300.
2. Basara, B., et al. (2001) On the calculation of external aerodynamics: industrial benchmarks, SAE Paper No. 2001-01-0701.
3. Bernard, P.S. and Wallace, J.M. (2002) *Turbulent Flow: Analysis, Measurement and Prediction*, John Wiley & Sons.
4. Bernard, P. S., et al. (2003) Studies of turbulent mixing using the VorCat implementation of the 3D vortex method, AIAA Paper No. AIAA-2003-3599.
5. Bernard, P. S., et al. (2004) Gridfree Simulation of Turbulent Boundary Layers Using VorCat, AIAA Paper AIAA-2003-3424.
6. Chorin, A. J. (1993) Hairpin removal in vortex interactions II, *J. Comput. Phys.* **107**, 1 - 9.
7. Duncan, B. D., et al. (2002) Numerical simulation and spectral analysis of pressure fluctuations in vehicle aerodynamic noise generation, SAE Paper No. 2002-01-0597.

8. Greengard, L. and Rokhlin, V. (1987) A fast algorithm for particle simulations, *J. Comput. Phys.* **73**, 325-348.

9. Krajnovic, S. and Davidson, L. (2001) Large-eddy simulation of the flow around a ground vehicle body, SAE Paper No. 2001-01-0702.

10. Lienhart, H. Stoots, C. and Becker, S. (2000) Flow and turbulence structures in the wake of a simplified car model (Ahmed model), *DGLR Fach. Symp. Der AG STAB*, Stuttgart Univ.

11. Morel, T. (1978) Aerodynamics drag of bluff body shapes characteristic of hatch-back cars, SAE Paper 780267.

12. Puckett, E. G. (1993) Vortex methods: an introduction and survey of selected research topics, in *Incompressible computational fluid dynamics: trends and advances*, edited by M. D. Gunzburger and R. A. Nicolaides, Cambridge University Press, Cambridge, pp. 335-407.

13. Spalart, P.R. (1988) Direct simulation of a turbulent boundary layer up to  $Re_\theta = 1410$ , *J. Fluid Mech.* **187**, 61-98.

14. Strickland, J. H. and Baty, R. S. (1994) A three-dimensional fast solver for arbitrary vorticity distributions, Report SAND93-1641, Sandia National Laboratory.

15. Uhlman, J. S. (1992) An integral equation formulation of the equations of motion of an incompressible fluid, Tech. Report 10086, NUWC-NPT.

16. Verzicco, R., et al (2002) Large eddy simulation of a road vehicle with drag-reduction devices, *AIAA J.* **40**, 2447-2455.

17. Zhang, Y. J., et al. (2003) A hybrid unstructured finite-volume algorithm for road vehicle flow computations with ground effects, *J. Vehicle Des.* **33**, 365 - 380.

## CONTACT

Please address inquiries to Peter Bernard at [bernard@umd.edu](mailto:bernard@umd.edu).